Supplementary material for "Photon-number-resolving aluminum kinetic inductance detectors"

X. Dai[1], H. Wang[2], Y. Wang[1,a)], Z. Mai[1], Z. Shi[1], Y-F. Wang[1], H. Jia[2], J. Liu[2], Q. He[3], M. Dai[3], P. Ouyang[3], Y. Chai[3], L-F. Wei[3], L. Zhang[4], Y. Zhong[2,5], W. Guo[2,a)], S. Liu[2,5], and D. Yu[2,5]

1) Quantum Optoelectronics Laboratory, School of Physical Science and Technology, Southwest Jiaotong University, Chengdu 610031, China

2) International Quantum Academy, Shenzhen 518048, China

3) Information Quantum Technology Laboratory, School of Information Science and Technology, Southwest Jiaotong University, Chengdu 610031, China

4) School of Electronic Science and Engineering, Nanjing University, Nanjing 210023, China

5) Shenzhen Institute for Quantum Science and Engineering, Southern University of Science and Technology, Shenzhen 518055, China

[a)] *Authors to whom correspondence should be addressed: Y. Wang, qubit@swjtu.edu.cn; W. Guo, guoweijie@iqasz.cn*

(Dated: December 24, 2024)

A. Device fabrication

The devices are all fabricated on high-resistivity ($>$ 10000 Ω·cm) and double-polished silicon wafer. Before film deposition, the silicon substrate is ultrasonically cleaned in acetone and isopropanol, followed by immersion in piranha solution (a mixture of concentrated sulfuric acid and hydrogen peroxide) to remove organic residues, and then cleaned by hydrofluoric acid to remove oxide layer on the silicon surface. After the substrate cleaning, a layer of SiN_x ($\sim$ 18 nm) is grown on the silicon using plasma enhance chemical vapor deposition (PECVD) technique. We then deposit aluminum (Al) film in an environment with a vacuum degree of 5×10^{-9} Torr using electron beam evaporation, and the deposition rate is about 0.5 nm/s. After defining the circuit pattern using a lift-off process, we deposit the top layer of SiN_x ($\sim$ 50 nm) over the entire wafer by PECVD. Both SiN_x layers are deposited at a lower temperature ≈ 80°C to avoid changes in the properties of the Al film.

The main DC properties of the fabricated devices are listed in Table S1. We obtain the resistivity and sheet resistance of the Al films by measuring the resistance of the feedline at room temperature. We obtain the sheet kinetic inductance of the Al film by comparing the measured resonance frequencies to their designed values. We measure T_c using a PPMS (Physical Property Measurement System) with helium-3 refrigerator, showing that $T_c \approx$ 1.2 K and the thicker Al film (25 nm) has a lower $T_c \approx 1.19$ K compared to $T_c \approx 1.25$ K for the thinner Al film (15 nm). We did not measure T_c for 40 nm Al film. Two microscope images of the fabricated resonator (Detector D) are shown in Fig. S1.

TABLE S1: The main DC properties of the Al films for detector (B-D), including the film thickness, the resistivity ρ, the sheet resistance R_s, the sheet kinetic inductance L_k and the superconducting transition temperature T_c.

Detector	Thickness	ρ ($\mu\Omega$·cm)	R_s ($\Omega/\square$)	L_k (pH/$\square$)	T_c (K)
B	15 nm	6.3	4.20	2.23	1.25
C	25 nm	4.1	1.64	0.77	1.19
D	40 nm	3.6	0.87	0.42	/

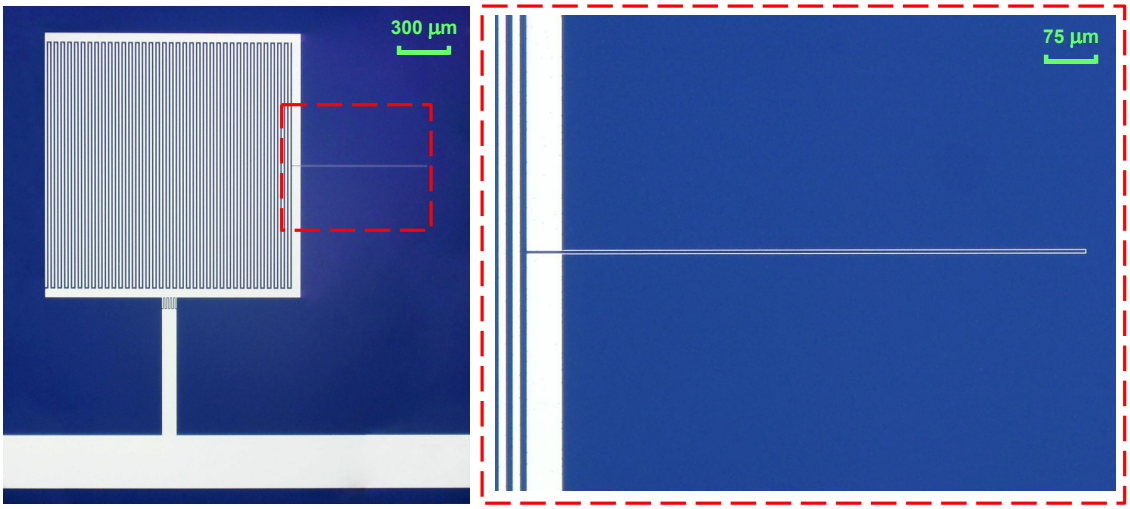

FIG. S1: [Color online] Microscope images of the lumped-element resonator. The figure on the right is an enlarged image of the inductor. The color of aluminum is white.

B. Fiber-to-detector coupling and alignment

Fig. S2(a) illustrates the complete fiber-to-detector assembly for manual alignment to increase the optical coupling. The assembly consists of a mounting base, a fiber-coupled collimator, a sample (detector) holder with moving platforms, and a microscope with a near-infrared camera (KEYENCE VH-5500). The sample holder is fixed to the base with screws, and the base is mounted on an optical breadboard. The fiber-coupled collimator is about 3 cm long and contains a lens which is customized to have a focal length of 3.5 mm at 1550 nm wavelength. A function generator is powered to stimulate a laser diode to produce a laser light of 1064 nm wavelength, which is sent into the fiber, focused by the lens, and illuminated onto the front side of the detector. Images of the transmission of the laser light through the detector and the substrate are acquired with the microscope camera. Note that the substrate is double-polished Si, which is transparent to light in the near-infrared wavelength range.

Fig. S2(b) is the exploded view of the sample holder, which is made of oxygen-free copper and consists of from bottom to top: the lower part, the middle part, the upper part, and the lid. The collimator can move along the Z-axis through the lower part and secure its position relative to the lower part with a few screws. The middle part is a moving platform which has two extruded guide rails matching the two slots on the lower part so it can move

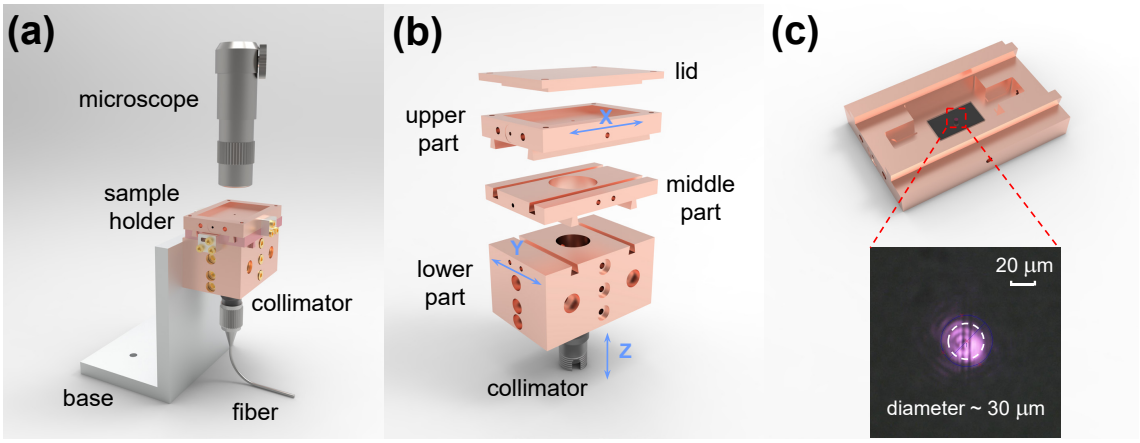

FIG. S2: [Color online] (a) The complete fiber-to-detector assembly for manual alignment. (b) The exploded view of the sample holder. (c) The incident light is focused onto the detector which is glued to the upper part of the sample holder. The recorded image of the transmission light through the detector and substrate shows a light spot of FWHM diameter ≈ 30 μm.

along the Y-axis. The position of the middle part relative to the lower part can be fixed by a few screws. Similarly, the upper part can move along the X-axis and can secure its position relative to the middle part. After manual alignment, a lid is placed on top of the upper part. Fig. S2(c) shows the bottom view of the upper part of the sample holder, where we can see the detector is glued to the bottom of the upper part with two SMA connectors (not shown) for microwave input and output. There is a small hole of diameter ≈ 1 mm allowing for light transmission in the middle of the upper part (not shown). By manually adjusting the positions of collimator and moving platforms, the area of the light spot on the detector can be minimized. Fig. S2(c) also shows an example image of the focused light spot (with a FWHM diameter ≈ 30 μm) relative to the inductive strip of the detector. It takes about 30 minutes for one manual alignment process.

C. Optical pulse response measurement

Our measurement setup for the homodyne detection scheme is shown in Fig. S3(a). A synthesizer generates a probe microwave signal at a certain frequency, which is divided into two signals through a power divider. One signal is used as a reference signal and input into the local oscillator (LO) port of the I/Q mixer (demodulator). The other signal is

attenuated before passing through the feed-line of the detector, amplified by a cryogenic amplifier (HEMT) and a room-temperature amplifier, and then input into the RF port of the IQ mixer. Inside the mixer, the RF and LO signals are both split, and the RF signals are mixed with two LO signals that have a 90 degree phase shift between them. The mixer outputs are then filtered by a low-pass filter (LPF) to remove the high-frequency mixing products, providing I and Q signals which are sampled at 2.5 Ms/s and converted to digital values by an analog to digital converter (ADC).

The sequence diagram of the optical pulse response measurement is sketched in Fig. S3(b), where two frames of pulse response are shown. A function generator drives a laser diode at room temperature to generate input optical pulses with a width of 200 ns at a repetition frequency of 120 Hz. The duration between two adjacent optical pulses is about 8.3 ms, which is long enough for the detector to relax to its initial state. The function generator also triggers the A/D converter. For each pulse, we collect 2 ms data centered at the trigger position as the response pulse and for calculating the template pulse in the following optimal filter processing. We also use the 2 ms pre-trigger data for the dark noise spectrum analysis.

D. Optimal pulse filtering

We apply the standard Weiner optimal filter to the measured frequency response pulses $V(t) = \delta f_r(t)/f_r$. A real pulse has the form $V(t) = AS(t) + N(t)$, with $V(t)$ the measured response pulse, $S(t)$ the template pulse, $N(t)$ the noise, and A the normalized pusle height to be estimated. In the frequency domain, we have $V(f) = AS(f) + N(f)$. A can be optimally estimated by calculating [1]:

$$A = \int_{-\infty}^{\infty} \frac{V(f)S^*(f)}{J(f)} \mathrm{d}f \Big/ \int_{-\infty}^{\infty} \frac{|S(f)|^2}{J(f)} \mathrm{d}f. \tag{S1}$$

In the integral of Eqn. S1, the lower frequency limit is 500 Hz, which is determined by the 2 ms duration of the response pulse (see Fig. S3(b)). The upper frequency limit is 1.25 MHz, which is equal to half of the sampling rate (2.5 MHz). $S(f)$ is calculated by Fourier transforming the template pulse $S(t)$, which is simply obtained by averaging all response pulses. $J(f) = |N(f)|^2/T$ ($T = 2$ ms) is the dark noise power spectral density (PSD), where $N(f) = \int_{-\infty}^{\infty} N(t)e^{-j2\pi ft}\mathrm{d}t$. $J(f)$ can be calculated from averaging the spectrum of each frame of 2 ms pre-trigger data with light off (see Fig. S3(b)).

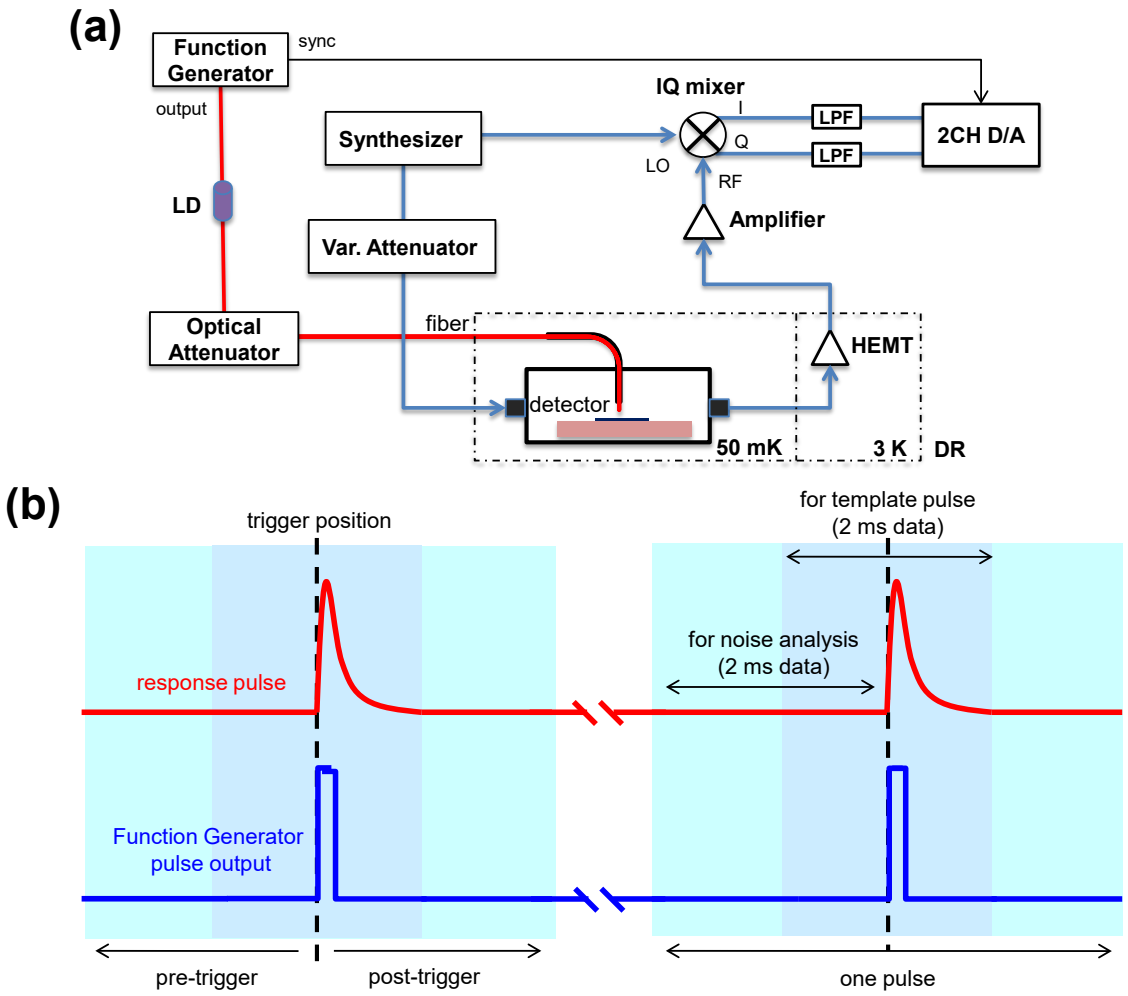

FIG. S3: [Color online] (a) Measurement setup for optical pulse response. (b) Sketched sequence diagram of the optical pulse response measurement.

As an example, Fig. S4(a) shows 18 unfiltered response pulses, which are randomly selected from a total of 20000 response pulses at a certain optical power. The average pulse of all 20000 response pulses, i.e., the template pulse $S(t)$ is shown in the inset of Fig. S4(a). The calculated PSD of the template pulse $|S(f)|^2/T$ and dark noise $J(f)$ are shown in Fig. S4(b). To check the consistency, we also plot the average residual, i.e., the average spectrum of each response pulse subtracting the corresponding optimally filtered pulse, showing good agreement with $J(f)$. The inset shows the zoom-in picture, where we can see the average residual is slightly bigger than $J(f)$. This deviation may attribute to the increasing frequency noise as away from resonance point. We will provide further discussion in Section E in the supplementary material.

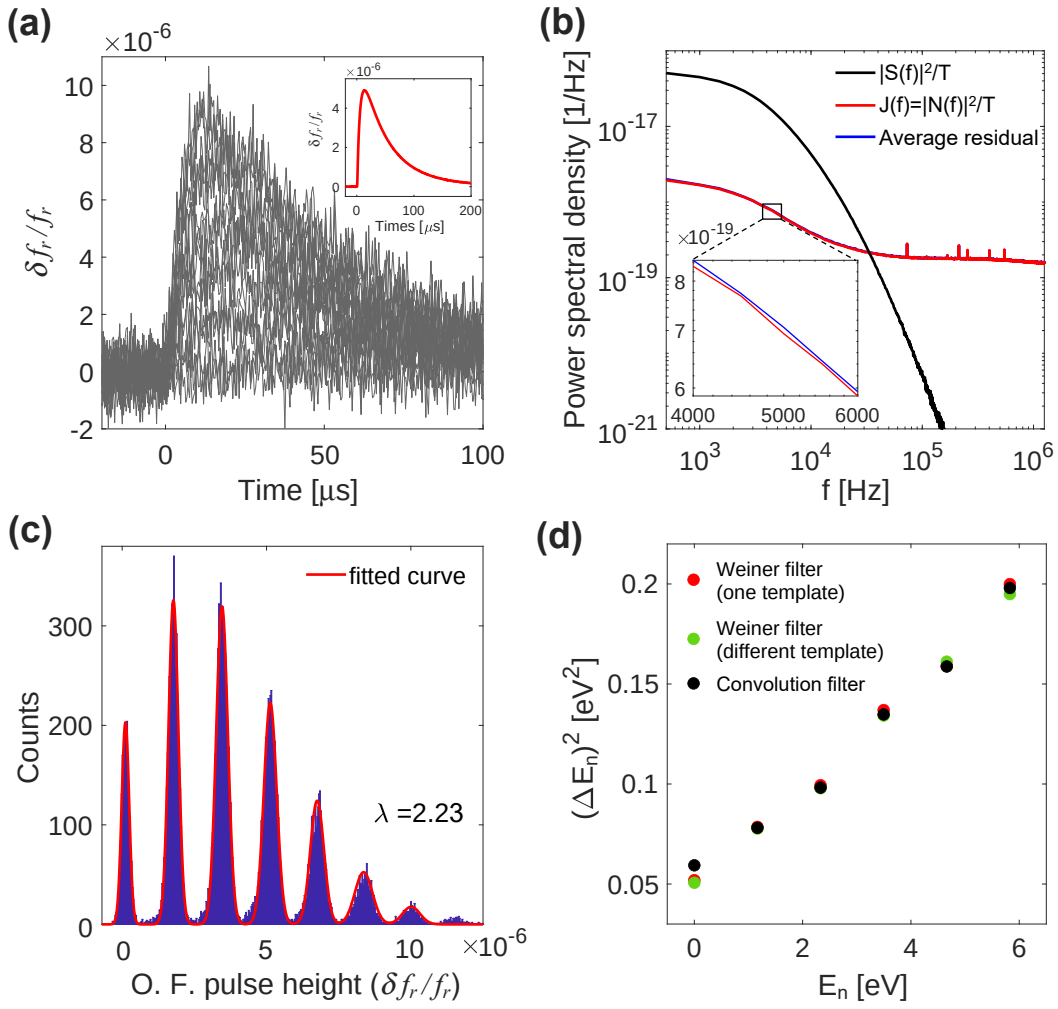

FIG. S4: [Color online] (a) Unfiltered frequency response pulses. (b) The calculated $|S(f)|^2/T$, $J(f)$, and average residual. (c) Photon-counting histogram with $\lambda = 2.23$. (d) The obtained ΔE_n^2 with absorbed photon energy are similar by using different optimal filtering methods.

The optimally filtered pulse height in $\delta f_r/f_r$ is given by $A \times H$, where H is the amplitude of the template pulse $S(t)$. Fig. S4(c) shows the histogram of $A \times H$, corresponding to a mean photon number $\lambda = 2.23$. The square of energy resolution ΔE_n^2 of each photon peak ($n = 0 - 5$) is shown as the red dots in Fig. S4(d), exhibiting a linear relation with the absorbed photon energy. Considering the response pulses for different photon number may have different pulse shapes, we also apply different template pulses to response pulses with different absorbed photon number. Besides, we also use a convolution filter without discrete Fourier transform for pulse filtering. As shown in Fig. S4(d), similar results are obtained with these three optimal filters.

E. Energy resolution due to dark noises

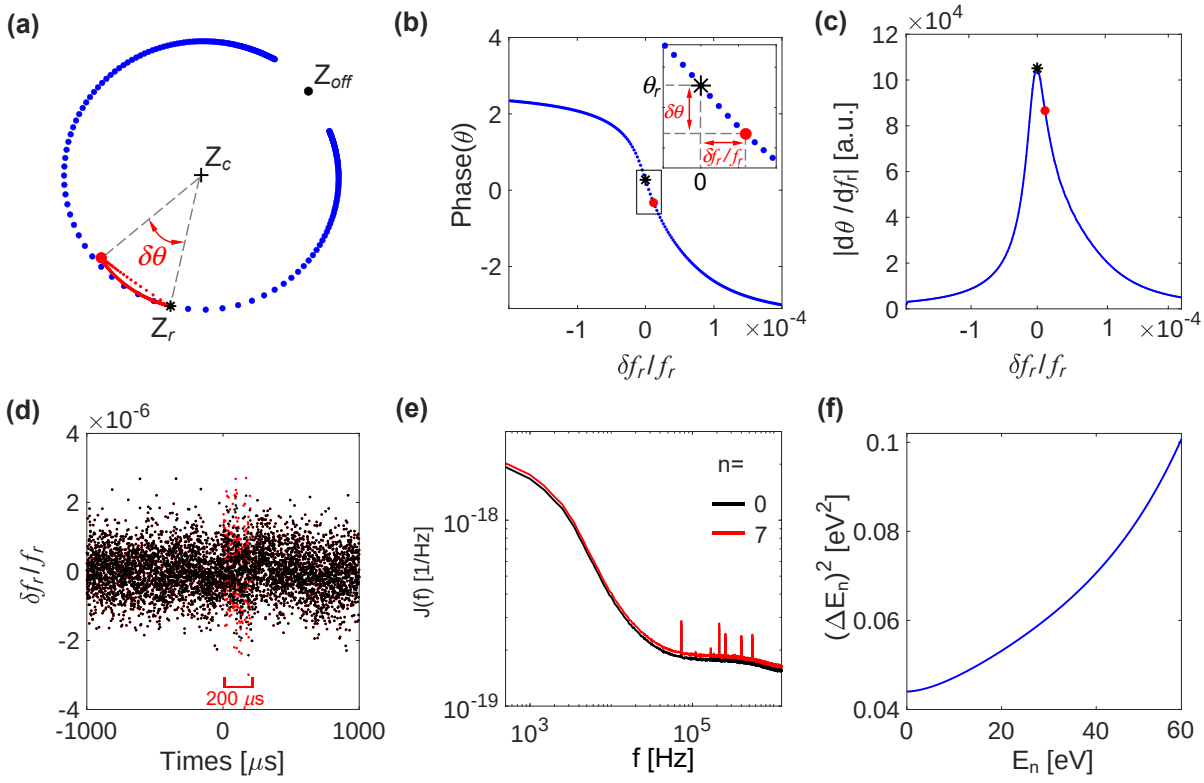

FIG. S5: [Color online] (a) The resonance circle (blue dots) and a response pulse (red dots) corresponding to $n = 7$ in the complex plane. (b) Phase angle θ as a function of the resonance frequency shift $\delta f_r/f_r$. (c) $|\mathrm{d}\theta/\mathrm{d}f_r|$ is maximized at resonance point and decreases with increasing $|\delta f_r/f_r|$, leading to a higher frequency noise away from the resonance point. (d) The modified noise (red) vs the dark noise (black) in the time domain. In the range of $0 - 200$ μs, the modified noise has a larger amplitude, which is determined by the response pulse amplitude. (e) $J(f)$ for $n = 7$ is slightly larger than $J(f)$ for $n = 0$. (f) The calculated upper limit of $\Delta E_{ns}(n)^2$, which is much smaller than experimental ΔE_n^2.

Here, we use a simple method to estimate the upper limit of $\Delta E_{ns}(n)$. Fig. S5(a) illustrates a resonance curve (S_{21}) and a response pulse in the complex plane. The pulse quickly deviates from the resonance point (Z_r), reaches its peak and then slowly relaxes back to Z_r with time. Through the phase-frequency relationship from the measured S_{21} (Fig. S5(b)), we can convert the phase change $\delta\theta$ to the frequency change δf_r, which is proportional to the absorbed photon number (energy) and taken as the response signal for

further processing. Assuming a given voltage noise (phase noise $\delta\theta$) due to amplifier and because $\delta f_r = \delta\theta/(\mathrm{d}\theta/\mathrm{d}f_r)$, the frequency noise is minimized at point Z_r, where the absolute value of $\mathrm{d}\theta/\mathrm{d}f_r$ is a maximum. As shown in Fig. S5(c), $|\mathrm{d}\theta/\mathrm{d}f_r|$ decreases as away from Z_r, therefore we expect that $\Delta E_{ns}(n)$ will increase with the absorbed photon energy $E_n = nh\nu$.

We can derive the variance of the O. F. pulse height $A \times H$, which takes the form [1]:

$$\sigma^2_{A\times H}/H^2 = \left[\int_{-\infty}^{\infty} \frac{|S(f)|^2}{J(f)}\mathrm{d}f\right]^{-1}. \tag{S2}$$

However, it is difficult to obtain $J(f)$ exactly because $J(f)$ varies with the response pulse height. For simplicity, we consider modifying the time-domain dark frequency noise $N(t)$ by amplifying a duration of 200 μs (about three times the relaxation time of the response pulse) noise to the noise amplitude at the response pulse peak (scaling with $1/|\mathrm{d}\theta/\mathrm{d}f_r|$), which is shown in Fig. S5(d). This allows us to estimate $J(f)$ (Fig. S5(e)) and $\sigma^2_{A\times H}$. By using Eqn. (1) in the manuscript, we can estimate $\Delta E_{ns}(n)^2$, which is plotted as the blue curve in Fig. S5(f). It shows that $\Delta E_{ns}(n)^2$ is much smaller than experimental ΔE_n^2.

F. Energy resolution due to current non-uniformity

Fig. S6(a) shows the simulated current density distribution at the resonance frequency $\approx$ 1 GHz for Detector C and we can see that the current is mainly distributed on the inductor strip. The phase velocity on the inductor is calculated to be $\approx 1.2 \times 10^8$ m/s, thus the microwave wavelength at 1 GHz $\approx$ 117 mm, which is much longer than the length of inductor strip $l_{ind} = 1.5$ mm. Therefore the current is expected to be very uniform on the inductor. This can be seen more clearly in Fig. S6(b), which shows that the difference in the current density is less than 0.2% on the entire inductor.

Non-uniform current distribution will lead to a position-dependent response, which contributes ΔE_{rsp} to the total energy resolution. Here we use a simple model to estimate ΔE_{rsp}. Let $I(x)$ $(0 < x < l_{ind})$ represent the simulated current density on the quasi-one-dimensional inductor strip, and $P(x)$ represent the probability of the photon being absorbed at position x, i.e., $P(x)$ is proportional to the spatial distribution of the illumination intensity. Without considering the quasi-particle diffusion, and assuming the single-photon response amplitude $A(x)$ for a photon absorbed at x is proportional to both the square of the current density $I^2(x)$ [2] and the single-photon energy $h\nu$, we have

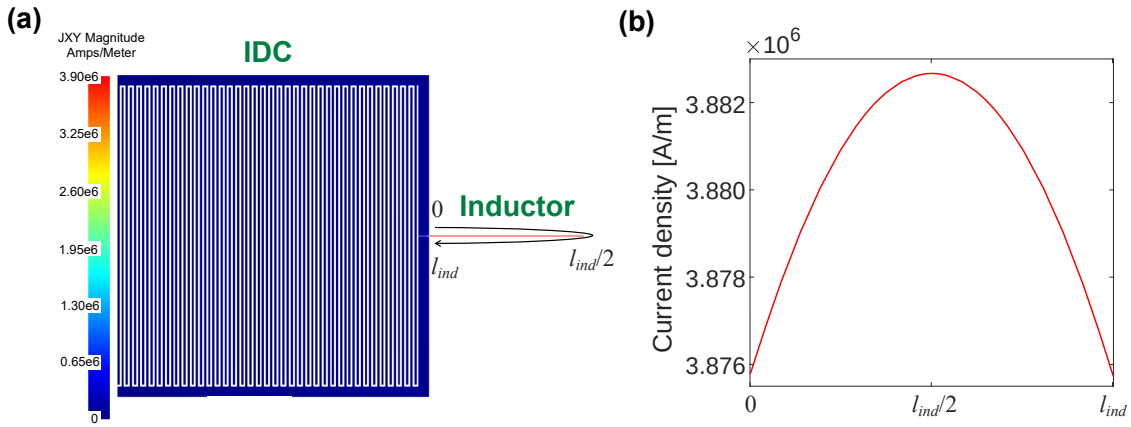

FIG. S6: [Color online] (a) Simulated current density distribution on Detector C. (b) The current density on the quasi-one-dimensional inductor strip shows great uniformity.

$A(x) = kh\nu I^2(x)$, where k is a proportionality coefficient. We can obtain the average single-photon response $\bar{A} = \int_0^{l_{ind}} A(x)P(x)\mathrm{d}x = kh\nu H_1$, where $H_1 = \int_0^{l_{ind}} I^2(x)P(x)\mathrm{d}x$, and the variance of the single-photon response $\sigma_A^2 = \int_0^{l_{ind}} (A(x) - \bar{A})^2 P(x)\mathrm{d}x = (kh\nu)^2 H_2$, where $H_2 = \int_0^{l_{ind}} (I^2(x)P(x) - H_1)^2 P(x)\mathrm{d}x$. Both H_1 and H_2 are only related to the distribution of current density and illumination intensity. For absorption of n independent photons, we can derive that the average n-photon response $\bar{A}_n = n\bar{A}$ and the variance $\sigma_{A_n}^2 = n\sigma_A^2$. Then we can obtain the n-photon energy resolution due to non-uniform responses by calculating $\Delta E_{rsp}(n) = 2\sqrt{2\ln(2)}\sigma_{A_n} nh\nu/\bar{A}_n = 2\sqrt{2\ln(2)}\sqrt{n}h\nu\sqrt{H_2}/H_1$. With the simulated current distribution and a Gaussian light spot of FWHM diameter ≈ 198 μm, we get $\Delta E_{rsp}(n = 1) \approx 2.53 \times 10^{-4}$ eV (corresponding to single-photon energy-resolving power $R_1 = 4610$), which is much smaller than the experimental $\Delta E_1 = 0.28$ eV.

If we further consider a quasi-particle diffusion length L, the single-photon response can be estimated by simply averaging the position-dependent responses, $A(x) = \int_{x-L/2}^{x+L/2} kh\nu I^2(x')\mathrm{d}x'/L$. Assuming a response time of $\tau = 20$ μs and a quasi-particle diffusion constant in Al film $D = 20$ cm^2/s, we have $L = (D\tau)^{1/2} = 200$ μm. The calculated $\Delta E_{rsp}(n = 1) \approx 2.51 \times 10^{-4}$ eV, which remains unchanged compared to the case without diffusion. This shows that the diffusion has little influence on the energy resolution as long as the diffusion length is much smaller than the inductor length.

The above analysis is based on ideal conditions. Under non-ideal conditions (e.g., imperfect film and device fabrication), the uniformity of current distribution may decrease

and lead to a more pronounced non-uniform response. If non-uniform response is indeed a main factor to limit energy resolution, we will find that $\Delta E_n^2 \sim (h\nu)nh\nu$. In other words, ΔE_n^2 with $nh\nu$ should exhibit different slopes for absorbed photons of different wavelengths. However, the experimental ΔE_n^2 with $nh\nu$ show the same slope for 1550 nm and 1064 nm photons, suggesting that non-uniform response is unlikely to make a significant contribution to energy resolution.

G. Calculation of phonon loss factor J

We follow the method in Ref. [3] to calculate the absolute phonon loss factor $J = J_{\text{high}} + J_{\text{low}}$, where J_{high} and J_{high} are phonon loss factors from high-energy part (from photon energy to around Debye energy Ω_D) and low-energy part (from Ω_D to characteristic energy $\Omega_1 \approx 10.6\Delta$ for Al) of the energy down-conversion process respectively.

For calculation of J_{high}, we take the equation (25) in Ref. [4] and reproduce it in Eqn. (S3) shown below:

$$\begin{aligned} J_{\pm}^{s} =& \frac{4\Omega_D}{\varepsilon_0} \sum_{m=0}^{\infty} \frac{\kappa\left(m^2\zeta^2\right)}{(1+\delta_{m,0})} \\ & \times \frac{(-1)^{m[s+(1\pm1)/2]}\{1-\exp[im\pi - d/L(E)]\}}{\{1-\exp[-d/L(E)]\}\left[1+m^2\pi^2L^2(E)/d^2\right]} \\ & \times \int_0^{\Omega_D} \frac{d\epsilon}{\Omega_D} \left(\frac{\epsilon}{\Omega_D}\right)^4 \frac{l_{pb}(\epsilon)}{d} \int_{\xi_c^{\pm}}^{1} d\xi\xi\eta_{\pm}(\xi) \\ & \times \left(\frac{1-\exp\left[im\pi - d/l_{pb}(\epsilon)\xi\right]}{1+m^2\pi^2 l_{pb}^2(\epsilon)\xi^2/d^2} \right. \\ & \left. -\eta_{\pm}(\xi)p_{\pm}(\xi)\frac{2\left\{1-\exp\left[im\pi - 2d/l_{pb}(\epsilon)\xi\right]\right\}}{4+m^2\pi^2 l_{pb}^2(\epsilon)\xi^2/d^2} \right). \end{aligned} \tag{S3}$$

In Eqn. (S3), $\kappa(x) = \exp(-x)\sinh(x)/x$, $\zeta^2 = \pi^2 D t_{dc}/2d^2$, $\delta_{m,m'}$ is the Kronecker symbol, $L(E)$ is the $1/e$ photon absorption depth, and $l_{pb}(\epsilon) = l_{pe,D}\frac{\Omega_D}{\epsilon}$ is the phonon mean free path [5]. $l_{pe,D}$ is determined by the Deybe phonon lifetime (≈ 3.5 ps in aluminum [6]) and average phonon velocity (≈ 3661 m/s in aluminum [7]). Other main notations and their input values are summarized in Table S2. For our case, we calculate $J_{\text{high}} = J_{-}$ with $s = 1$, because the photon is incident onto the top surface of the Al absorber and the hot phonons are lost from the substrate below the absorber. We use the same material parameters for Al film as in Ref. [3]. For high-resistivity Si (100) substrate, we take the longitudinal phonon

TABLE S2: The notations and input values to calculate J.

Notations	Definitions	Values
Ω_D	Debye energy	36.9 meV
Ω_1	characteristic energy	10.6Δ
ε_0	mean energy necessary to generate a single QP	1.7Δ
s	$s = 1$ (2) for photon incident from the top (bottom)	1
D	the QP diffusion coefficient	2e-3 $\mathrm{m^2 s^{-1}}$
t_{dc}	duration of E_1 to Ω_D stage	4.5e-14 s
d	thickness of the Al absorber layer	25 nm
$l_{pe,D}$	mean free path of phonons with Debye energy	12.8 nm
ξ_c	cosine of the critical angle for phonon transmission at the interface	0.629
η	transmission coefficients for phonons at the interface	0.63
p	probability of phonon reaching an interface without being absorbed	0.185

velocity $c_l = 8556$ m/s and transverse phonon velocity $c_t = 3260$ m/s from Ref. [8]. This results in the cosine of the critical angle for phonon transmission at the interface $\xi_c^- = 0.890$, the probability of phonon reaching an interface without being absorbed $p_- = 0.185$, and the transmission coefficients for phonons at the Al/Si interface $\eta_- = 0.63$ [7]. With these parameters we obtain $J_{\mathrm{high}} = 2.3$. Note that there is a 18 nm thin SiN_x layer between Al and Si substrate. If we use the properties of SiN_x film ($c_l = 10300$ m/s and $c_t = 6200$ m/s) as in Ref. [3] to calculate Eqn. (S3), we will obtain $J_{\mathrm{high}} = 1.5$.

For calculation of J_{low}, we use the Eqn. (C1) in Ref. [3] and obtain $J_{\mathrm{low}} = 0.9$ (0.5) for Si (SiN_x) substrate. Therefore we estimate $J = J_{\mathrm{high}} + J_{\mathrm{low}} = 2.3 + 0.9 = 3.2$ for our device (detector C).

H. Determination of photon number

As shown in the histograms of Fig. 3 in the manuscript, the photon counting events obey Poisson statistics. With increasing mean photon number λ, the distribution shifts to higher photon numbers and more photon peaks can be observed. At higher optical powers, as is the case in Fig. 5 in the manuscript, the first few photon peaks can not be seen.

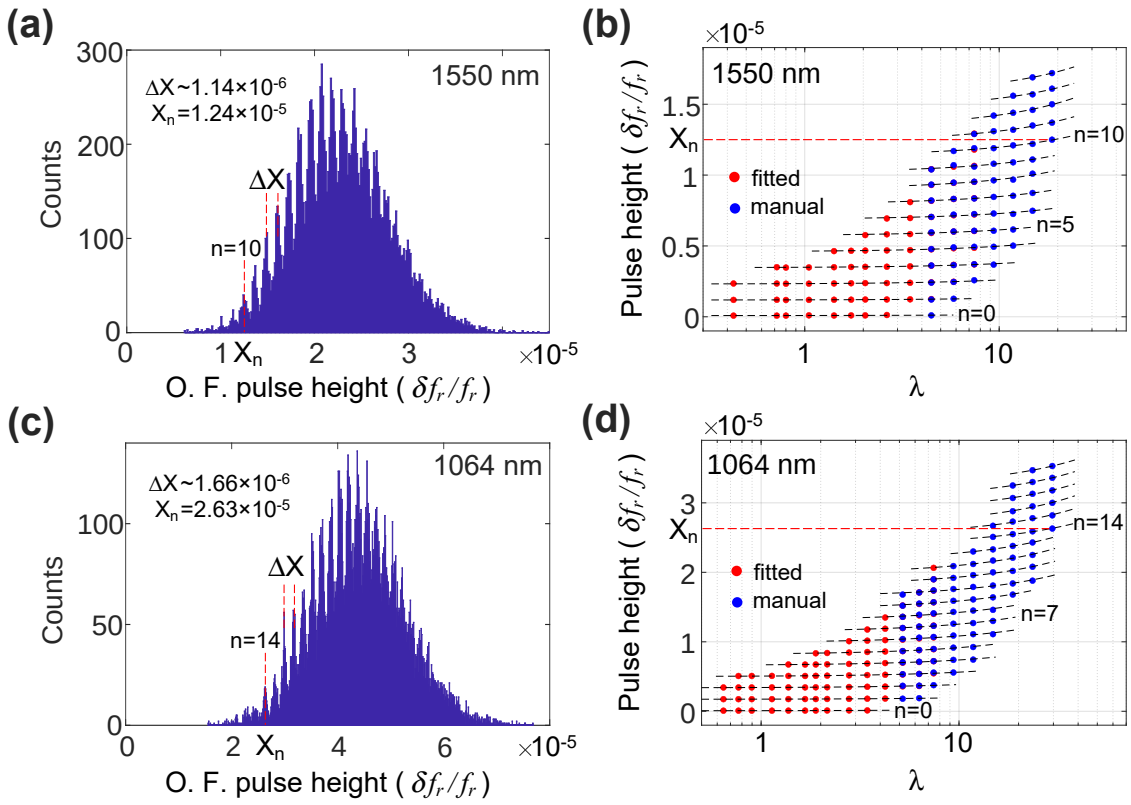

FIG. S7: The method to determine the photon number of each photon peak. (a) Photon-counting histogram at 1550 nm. (b) Pulse height of clearly visible photon peaks as a function of λ at 1550 nm. (c) Photon-counting histogram at 1550 nm. (d) Pulse height of clearly visible photon peaks as a function of λ at 1550 nm.

To determine the photon number n of each photon peak in Fig. 5, we can calculate $n \sim X_n/\Delta X$, where X_n is the n-photon peak position (in O. F. pulse height) and ΔX is the spacing between adjacent photon peaks. In all histograms, we can see ΔX is the same, corresponding to a fixed single-photon responsivity $(\delta f_r/f_r)_{n=1} = \Delta X \approx 1.66 \times 10^{-6}$ for 1064 nm and $\Delta X \approx 1.14 \times 10^{-6}$ for 1550 nm. For the marked photon peaks in Fig. S7(a) and Fig. S7(c), we get $n \approx 10.88$ and $n \approx 15.84$ respectively, which are generally not integers.

To further determine the photon number, we show the pulse height of clearly visible photon peaks as a function of mean photon number in Fig. S7(b) and Fig. S7(d). For lower λ, we obtain the pulse height (red dots) from fitting. We manually determine the pulse height (blue dots) for higher λ due to the difficulty in fitting. In some areas, we see the overlap of red and blue dots, indicating that the manually determined pulse height is close

to the value obtained from fitting. The data points clearly fall into different groups (marked by the dashed lines), corresponding to different photon numbers n. We can then determine the photon number for each photon peak. Note that the pulse height is flat with λ for lower n, and increases a little with λ for higher n due to the possible IDC response and thermal effects at higher optical powers.

---

[1] S. R. Golwala, Ph.D. thesis, University of California, Berkeley, 2000.

[2] X. Dai, X. Liu, Q. He, Y. Chen, Z. Mai, Z. Shi, W. Guo, Y. Wang, L. Wei, M. Vissers, and J. Gao, Supercond. Sci. Technol. **36**, 015003 (2023).

[3] P. Visser, S. Rooij, V. Murugesan, D. Thoen, and J. Baselmans, Phys. Rev. Appl. **16**, 034051 (2021).

[4] A. G. Kozorezov, J. K. Wigmore, D. Martin, P. Verhoeve, and A. Peacock, Phys. Rev. B **75**, 094513 (2007).

[5] A. G. Kozorezov, A. F. Volkov, J. K. Wigmore, A. Peacock, A. Poelaert, and R. den Hartog, Phys. Rev. B **61**, 11807 (2000).

[6] S. B. Kaplan, C. C. Chi, D. N. Langenberg, J. J. Chang, S. Jafarey, and D. J. Scalapino, Phys. Rev. B **15**, 3567 (1977).

[7] Steven B. Kaplan, J. Low Temp. Phys. **37**, 343 (1979).

[8] S. Wang, Y. Hsu, J. Pu, J. Sung, and L. Hwa, Materials Chemistry and Physics **432**, 85 (2004).